RSC Advances

PAPER

View Article Online
View Journal | View Issue

Cite this: *RSC Adv.*, 2024, **14**, 12255

Catalytic pyrolysis and *in situ* carbonization of walnut shells: poly-generation and enhanced electrochemical performance of carbons

Wenjing He,[ab] Keling Liu,[a] Lanjun Zhang,[ab] Muxin Liu,[c] Zhengjie Ni,[a] Yueyang Li,[a] Duoduo Xu,[a] Minjie Cui[d] and Yibo Zhao*[ab]

In this study, walnut shell (WS) was used as feedstock, incorporating lithium carbonate (LC), sodium carbonate (SC), potassium carbonate (PC), and potassium hydroxide (PH) as pyrolysis catalysts and carbonization activators. A one-step method that allows catalytic pyrolysis and carbonization to be carried out consecutively under their respective optimal conditions is employed, enabling the concurrent production of high-quality pyrolysis oil, pyrolysis gas, and carbon materials from biomass conversion. The effects of LC, SC, PC, and PH on the yield and properties of products derived from WS pyrolysis as well as on the properties and performance of the resulting carbon materials were examined. The results indicated that the addition of LC, SC, PC, and PH enhanced the secondary cracking of tar, leading to increased solid and gas yields from WS. Additionally, it increased the production of phenolic compounds in bio-oil and H_2 in syngas, concurrently yielding a walnut shell-based carbon material exhibiting excellent electrochemical performance. Specifically, when PC was used as an additive, the phenolic content in the pyrolysis oil increased by 27.64% compared to that without PC, reaching 74.9%, but the content of ketones, acids, aldehydes, and amines decreased. The hydrogen content increased from 2.5% (without the addition of PC) to 12.75%. The resulting carbon (WSC–PC) displayed a specific surface area of 598.6 $m^2\ g^{-1}$ and achieved a specific capacitance of 245.18 F g^{-1} at a current density of 0.5 A g^{-1}. Even after 5000 charge and discharge cycles at a current density of 2 A g^{-1}, the capacitance retention rate remained at 98.16%. This method effectively enhances the quality of the biomass pyrolysis oil, gas, and char, contributing to the efficient and clean utilization of biomass in industrial applications.

Received 1st March 2024
Accepted 6th April 2024

DOI: 10.1039/d4ra01608d

rsc.li/rsc-advances

Introduction

Energy and environmental issues are global priorities. China is rich in coal but poor in oil and gas, relying heavily on coal, which accounts for 56.2% of its energy in 2022. However, coal usage poses severe environmental problems. Biomass energy, which has the advantages of being green, clean, readily available, sustainable, and emitting zero carbon dioxide, is considered a potential substitute for fossil fuels.[1] Extensive research has been conducted on biomass processing and utilization technologies,[2–6] with biomass pyrolysis being a key focus. Pyrolysis converts biomass into solids (pyrolysis char), liquids (pyrolysis oil), and gases (pyrolysis gas) under high-temperature and oxygen-free conditions. Owing to its mild reaction conditions and versatility with various feedstocks, it is extensively studied globally. Current research in biomass pyrolysis technologies focuses on two key aspects. Firstly, efforts aim to improve the yield and quality of the pyrolysis liquid by altering the pyrolysis methods and conditions. Secondly, the production of carbon materials through pyrolysis technology has been explored, along with their modification for various applications, such as adsorption,[7,8] catalysis,[6] and energy storage.[9] However, it has become common to focus on only one aspect, such as improving liquid or gas quality, often neglecting solid products or concentrating on carbon modification and overlooking comprehensive research on liquid and gas products.

In recent years, there has been growing interest in co-producing biomass pyrolysis technology owing to its potential to enhance the overall efficiency of biomass conversion. However, the tar produced from biomass pyrolysis has certain drawbacks, including high oxygen content, low calorific value, and high viscosity.[10] Additionally, the obtained solid products have a relatively small specific surface area, which limits their application potential. Consequently, researchers have employed various strategies to improve the quality of the

[a]School of Environmental and Chemical Engineering, Jiangsu Ocean University, Lianyungang, Jiangsu 222005, China
[b]Jiangsu Institute of Marine Resources Development, Jiangsu Ocean University, Lianyungang 222005, China
[c]School of Materials and Chemical Engineering, Bengbu University, Bengbu, Anhui 233030, PR China
[d]Institute of Physics and Beijing National Laboratory for Condensed Matter Physics, Chinese Academy of Sciences, Beijing 100190, China

pyrolysis products, such as altering the pyrolysis temperature,[11,12] and atmosphere,[13] incorporating catalysts, and implementing biomass pretreatment.[14] Among these strategies, adding a catalyst offers significant advantages.

Catalysts not only facilitate high selectivity of desired target products during biomass pyrolysis but also enable the modification of product quality to meet specific requirements. Moreover, catalysts effectively lower the reaction temperature and energy consumption, thereby reducing equipment and operational costs. Alkaline catalysts are widely used in biomass pyrolysis because of their strong reversibility, high catalytic activity, good compatibility, and cost-effectiveness compared to other catalysts. Among alkaline catalysts, alkali metal carbonates offer the advantages of alkaline metal catalysts while also being recyclable and environmentally friendly. By adding alkaline catalysts during biomass pyrolysis, the distribution and composition of the resulting pyrolysis products can be enhanced. According to Zhou *et al.*,[15] potassium hydroxide (PH) and potassium carbonate (PC) can lower the activation energy of wood pyrolysis under different heating rates in a nitrogen atmosphere. These alkaline catalysts also promote the formation of char, indicating their role in facilitating the dehydrogenation and aggregation of large molecular aromatic hydrocarbons. Tirapanampai *et al.*[16] investigated the effects of sodium carbonate (SC) on the pyrolysis of microalgae in terms of both bio-oil composition and thermal behavior. These findings suggest that an appropriate catalyst and high temperature can decrease the carboxylic acid content in bio-oil while increasing levels of aromatics and nitrogen-containing compounds. Shen *et al.*[17] studied the catalytic pyrolysis of rice husks using PH, PC, and potassium oxalate (PO). The study demonstrated that the presence of potassium compounds shifted biomass decomposition to a lower temperature range, facilitating the *in situ* catalytic upgrading of bio-oil. This resulted in the production of bio-oils rich in hydrocarbon compounds and synthesis gas rich in H_2.

Alkaline catalysts also contribute to activating biomass pyrolysis char, optimizing performance by modifying the pore structure of the biochar. Jia *et al.*[18] employed a two-step process of hydrothermal pre-carbonization and PC activation, using cottonseed meal as the carbon precursor. This method produced self-doped heteroatoms and hierarchical porous carbon materials, exhibiting a remarkably high specific surface area of up to 2361 $m^2\ g^{-1}$, alongside outstanding energy and power density. PH, PC, and PO as activators for lignocellulosic residue char stimulate cracking, deoxygenation, dehydrogenation, and aromatization reactions, resulting in abundant micropores, and the electrode materials have been developed with excellent performance.[19] Furthermore, a mixture of lithium carbonate (LC), SC, and PC as activating agents results in a biomass char with a high specific surface area, making it a suitable candidate for efficient CO_2 adsorption.[20]

In this study, a one-step process was employed to integrate catalytic biomass pyrolysis and char activation. This method differs from the traditional one-step methods, where the reaction is typically carried out directly at a certain temperature for a specific duration.[21,22] Walnut shell (WS) was used as a raw material and mixed with LC, SC, PC, and PH in specific proportions. The influence of additives on the yield and properties of the pyrolysis products was investigated using a tube furnace, thermogravimetric analysis (TGA), gas chromatography-mass spectrometry (GC-MS), and gas chromatography (GC). Furthermore, the impact of additives on the structure and properties of carbon was examined using scanning electron microscopy (SEM), Brunauer–Emmett–Teller surface area analysis (BET), Fourier-transform infrared spectroscopy (FTIR), X-ray diffraction (XRD), Raman spectroscopy, and an electrochemical workstation. The aim of this work is to develop a simple and effective biomass processing method that can simultaneously enhance the quality of gas, liquid, and solid products.

Materials and methods

Materials

The WS was washed, dried, and then crushed and sieved to obtain particles ranging from 0.2 mm to 0.45 mm. After vacuum drying at 110 °C for 12 h, these particles were stored for subsequent use. The proximate and ultimate analysis of WS can be found in our previously published article.[23] LC (99.0% purity) and *N*-methyl-2-pyrrolidone (NMP, 99.0% purity) were obtained from Aladdin. SC (99.8% purity), PC (99.0% purity), and tetrahydrofuran (THF, 99.0% purity) were purchased from Tianjin Yongda Chemical Reagent Co., Ltd. PH (95.0% purity) was sourced from Shanghai Boer Chemical Reagent Co., Ltd. Hydrochloric acid (HCl, 36.0%) used was purchased from the China National Pharmaceutical Group Chemical Reagent Co., Ltd.

One-step pyrolysis-carbonization experiment

Before the experiment, 2 g of WS was thoroughly mixed with 0.5 g of X (X = LC, SC, PC, and PH), resulting in WS–LC, WS–SC, WS–PC, and WS–PH, respectively. The tube furnace preheated to 650 °C used nitrogen gas at a flow rate of 200 mL min^{-1} as the carrier gas. WS and WS–X samples were placed in a quartz boat, as shown in Fig. 1a. The quartz reactor containing samples was swiftly inserted into the tube furnace, positioning samples in the isothermal zone (Fig. 1b). The pyrolysis process concluded after 6 minutes, collecting pyrolysis tar and pyrolysis gas; no volatile components were generated. Subsequently, carbonization of pyrolysis char was conducted. The pyrolysis apparatus, samples, and tube furnace remained unchanged. The tube furnace was heated from 650 °C to 700 °C at a rate of 5 °C min^{-1}, held for 2 h, and cooled to room temperature; the produced carbon was removed. The carbon was then placed in a 1 mol L^{-1} HCl solution, stirred at 25 °C for 12 h, and washed with distilled water until the pH reached neutral, followed by vacuum drying at 80 °C for 12 h. The obtained WS-based carbon was named WSC, and corresponding samples with X were named WSC–X (WSC–LC, WSC–SC, WSC–PC, and WSC–PH).

It was not possible to obtain the yield of pyrolysis char in the above one-step pyrolysis-carbonization experiment. Therefore, a separate pyrolysis experiment was required to determine the yields of the pyrolysis products. In this pyrolysis experiment, the

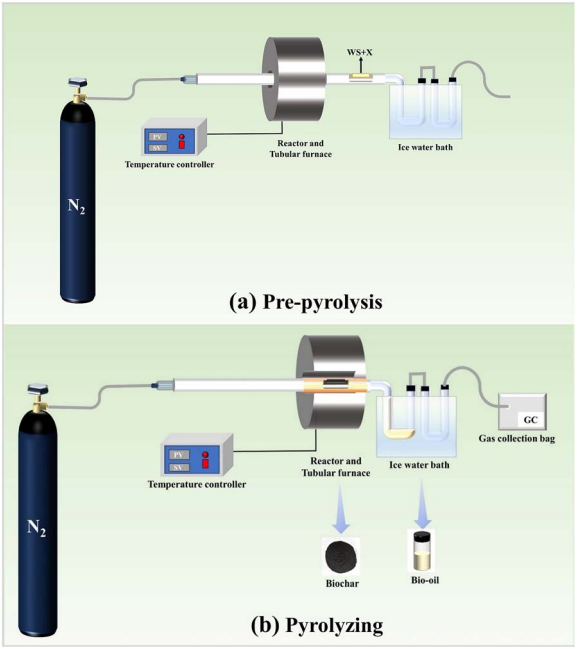

Fig. 1 Schematic diagram of the experimental process, before (a) and during (b) pyrolysis.

procedure concluded after 6 min at a temperature of 650 °C, and the pyrolysis product yield was calculated using the following formula:

Liquid product yield (Y_L)

$$Y_L = M_L/M \times 100\% \quad (1)$$

Solid product yield (Y_S):

$$Y_S = M_S/M \times 100\% \quad (2)$$

Gas product yield (Y_G) was obtained by subtraction:

$$Y_G = 100\% - Y_L - Y_S \quad (3)$$

where M represents the mass of the WS, M_L represents the mass of the liquid product, and M_S represents the mass of the pyrolysis char obtained at 650 °C.

Characterization of pyrolysis tar and gas

The chemical composition of the pyrolysis tar was analyzed using a GCMS-QP 2010 instrument (Shimadzu Corporation, Japan). The MS detector operated in full scan mode with a mass range (m/z) of 10 to 550 μm. The chromatographic column was a 30 m × 0.25 mm SH-Rxi-5 SiL MS column with a film thickness of 0.25 μm. The injector and detector temperatures were set at 300 °C and 280 °C, respectively.

The pyrolysis gas was analyzed using a GC-2010 gas chromatograph (Shimadzu Corporation, Japan). The column oven temperature was maintained at 60 °C, and the bridge current was set to 80 mA with a negative polarity. The injector temperature was set at 150 °C. Gas detection was performed using a flame ionization detector (FID) and a thermal conductivity detector (TCD) with helium as the carrier gas. The FID detector temperature was set at 250 °C, and the TCD detector temperature was set at 200 °C.

Additionally, TGA of the samples was performed using a NETZSCH STA 449 F3 instrument. A sample weighing 9 mg was heated in a nitrogen atmosphere at a rate of 10 °C min^{-1} from 30 to 750 °C to observe the changes in sample mass. It should be noted that, in order to maintain consistency with the pyrolysis conducted in the tube furnace, the weight (%) was calculated based on the mass of WS rather than the mass of the total sample (M_T). Therefore, the weight (%) measured directly (W_m) by TG needs to be adjusted using the following calculation formula.

$$\text{Weight}(\%) = 1 - \frac{M_T(1 - W_m)}{M} \quad (4)$$

Characterization of carbonized samples

The microstructures and surface morphologies of the carbonized samples were examined using SEM (Regulus 8100). N_2 adsorption–desorption isotherms were obtained at −196 °C using a high-performance surface area and pore size analyzer (3H-2000PM1). These isotherms were subsequently used to calculate the specific surface area (S_{BET}), total pore volume (V_{total}), micropore volume (V_{micro}), average pore diameter (D), and the pore size distribution was calculated according to the adsorption branch of the isotherm by using the NonLocal Density Functional Theory (NLDFT) model. The crystal structure of the carbon material was analyzed using an XRD (Bruker D8A) with a tube voltage of 40 kV and a tube current of 40 mA. The scanning speed was set at 5° min^{-1}, and the scanning angle ranged from 10° to 90°. The interlayer distance (d_{002}) was calculated using the (002) graphite diffraction peak and Bragg's formula eqn (5),[24] and Scherrer's formula was used to obtain the nanocrystalline height (L_c) and nanocrystalline width (L_a) as in eqn (6) and (7):[25]

$$d_{002} = \frac{\lambda}{2 \sin \theta_{002}} \quad (5)$$

$$L_c = \frac{K_c \cdot \lambda}{B_{002} \cdot \cos \theta_{002}} \quad (6)$$

$$L_a = \frac{K_a \cdot \lambda}{B_{100} \cdot \cos \theta_{100}} \quad (7)$$

where, $K_c = 0.9$, $K_a = 1.84$, λ is the X-ray wavelength (1.5406 Å), θ_{002} and θ_{100} are the Bragg's angles, B_{002} and B_{100} are the full width at half maximum (FWHM) of the (002) and (100) peaks, respectively.

The surface functional groups of the carbon materials were characterized using FTIR (Nicolet-iS10). Additionally, the structure of the carbon material was further investigated using Raman spectroscopy (Raman, LabRAM HR Evo) with an excitation wavelength of 532 nm and a scanning range of 500 to 2500 cm^{-1}.

The electrochemical performance of WSC–X (X = LC, SC, PC, or PH) was evaluated using an electrochemical workstation

(Shanghai Chenhua, CHI760E) employing cyclic voltammetry (CV), galvanostatic charge/discharge (GCD), and electrochemical impedance spectroscopy (EIS). The carbon electrode was prepared by grinding and mixing samples with Super P and polyvinylidene fluoride at a mass ratio of 8 : 1 : 1 in NMP. The resulting mixture was coated onto 1 cm × 1 cm nickel foam and vacuum-dried at 80 °C for 12 h, resulting in a sample loading of approximately 3–4 mg. The electrochemical tests were conducted in a 6 mol L^{-1} KOH electrolyte solution using Hg/HgO as the reference electrode and a platinum electrode as the counter electrode. The CV measurements were performed within a voltage window of −1 to 0 V at scan rates ranging from 5 to 200 mV s^{-1}. The GCD tests were performed at current densities ranging from 0.5 to 10 A g^{-1}. EIS measurements were performed over a frequency range of 10^{-2} to 10^{5} Hz with an amplitude of 5 mV.

The specific capacitance (C_m, F g^{-1}), based on the GCD curve in the three-electrode system, was calculated using the following equation:

$$C_m = I\Delta t/m\Delta V \quad (8)$$

where I is the discharge current (A), Δt is the discharge time (s), m is the loading mass of the active material (g), and ΔV is the potential range (V).

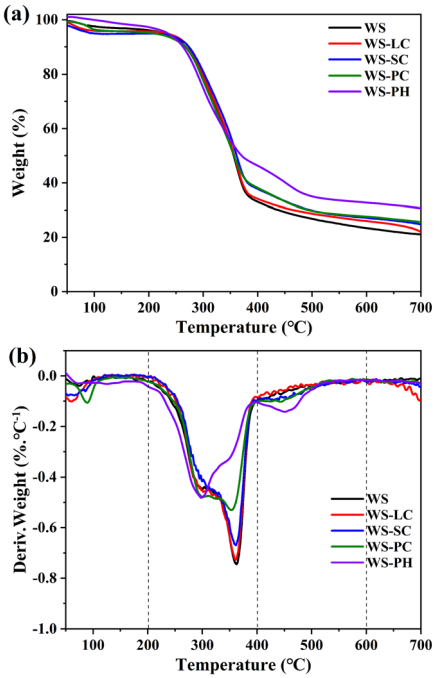

Fig. 2 (a) TG and (b) DTG curves of WS and WS–X (X = LC, SC, PC and PH).

Results and discussion

Analysis of pyrolysis product yield

The pyrolysis product yields of WS and WS–X (X = LC, SC, PC, or PH) are listed in Table 1. WS pyrolysis yielded 59.06%, 22.81%, and 18.13% of liquid, solid, and gas, respectively. Upon the addition of X, the liquid yield decreased, whereas the solid and gas yields increased. Furthermore, as the alkalinity of the additive increased, this phenomenon became more pronounced.

To further validate the aforementioned experiments and analyze the observed phenomena, thermal weight loss behavior was examined (Fig. 2). TGA curves revealed that the solid product yields of WS, WS–LC, WS–SC, WS–PC, and WS–PH at 650 °C were 23.72%, 26.59%, 27.73%, 27.74%, and 31.81%, respectively. These results align with those of the pyrolysis experiments. The differential thermogravimetry (DTG) curve of WS in individual pyrolysis exhibited two stages within the main pyrolysis temperature range (200–600 °C). In the first stage (200–400 °C), a shoulder peak attributed to hemicellulose and some lignin preceded the main peak, associated with cellulose and a small amount of lignin.[15] In the second stage (400–600 °C) the curve represented lignin pyrolysis. Specifically, the shoulder peak of WS–PH at around 440 °C may be attributed to the release of the potassium salt in the biochar.[26] Comparing individual WS pyrolysis to WS–LC and WS–SC, a shift in the shoulder peak temperature suggested that LC and SC inhibited hemicellulose decomposition. WS–PC and WS–PH DTG curves exhibited a low temperature for the main pyrolysis peak, and after the addition of PH, it can be seen that the decomposition temperature of walnut shell pyrolysis shifted from 360 °C to 300 °C, the maximum pyrolysis rate is greatly reduced. This phenomenon is attributed to the addition of potassium salts, which can lower both the pyrolysis temperature and activation energy of cellulose decomposition. This finding is consistent with those reported by Zhou[15] and Chen.[27] The addition of X reduces the maximum weight loss rate observed in the DTG curves. This decrease in weight loss can be attributed to the inhibitory effect of X on the volatilization of the components.[15] Additionally, alkali-catalyzed polymerization increases char production.[28]

Table 1 Yield distribution of pyrolysis products of WS under different additives

	Yields/%		
Samples	Liquid	Solid	Gas
WS	59.06	22.81	18.13
WS–LC	46.36	27.46	26.18
WS–SC	42.44	28.02	29.54
WS–PC	41.85	28.1	30.05
WS–PH	40.47	29.03	30.5

Liquid component analysis

The GC-MS results of WS pyrolysis tar are shown in Fig. 3. For clarity, liquid pyrolysis products were categorized into functional groups, including phenols, ketones, esters, acids, aldehydes, amines, and others (hydrocarbons, thiophenes, ethers, nitrogen-containing compounds, *etc.*).

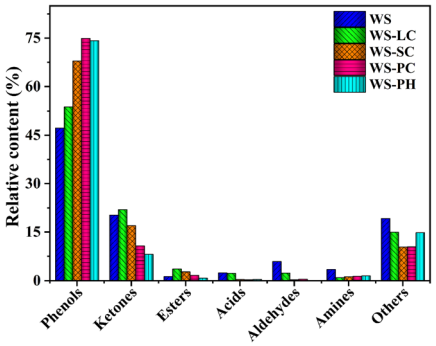

Fig. 3 GC-MS analysis of bio-oil fractions.

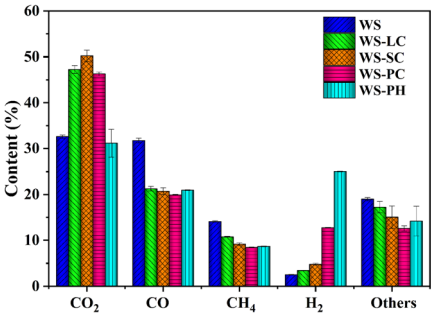

Fig. 4 Analysis of gas components.

As shown in Fig. 3, the main component of the liquid products of pyrolysis were primarily monocyclic phenolic compounds. The addition of LC, SC, PC, and PH to the WS pyrolysis process led to a significant increase in the phenolic compound content. Specifically, the content of phenolic compounds increases from 47.26% in the sole pyrolysis to 53.77%, 67.88%, 74.9%, and 74.24% with the addition of LC, SC, PC, and PH, respectively. Among these compounds, the content of alkylphenols exhibited the most notable increase, rising from 8.26% in the sole pyrolysis to 9.57%, 23.53%, 36.18%, and 35.13%. The content of alkoxylphenols also increased, ranging from 16.14% in the sole pyrolysis to 24.03%, 26.84%, 21.68%, and 24.41%. However, the content of phenolic compounds containing both alkoxyl and alkyl groups decreases from 20.01% in the sole pyrolysis to 19.91%, 17.51%, 16.63%, and 14.7%. The increase in phenolic compound content suggests that the addition of catalysts can facilitate the cleavage of C–C and C–O bonds between the phenylpropane monomers in lignin, leading to the release of phenolic monomers.[29] Additionally, due to their larger ionic radius and lower charge density, potassium ions are more likely to form coordination bonds, thereby altering the electron density distribution and reaction activity, making C–C or C–O bonds more susceptible to cleavage. Hence, the addition of potassium salts as catalysts resulted in the most significant increase in phenolic compound content. The notable increase in the content of alkylphenols in the products can be attributed to the strong deoxygenation and decarbonylation effects of alkaline catalysts. The increase in the content of alkoxylphenols is expected to be related to the overall increase in phenolic compound content. Similarly, the decrease in the content of phenolic compounds containing both alkoxyl and alkyl groups was also attributed to the deoxygenation by alkaline catalysts, resulting in their conversion into alkylphenols. The addition of additives led to a significant reduction in ketones, acids, aldehydes, and amines in the bio-oil. The decrease in acid compounds can be attributed to the enhanced cleavage of carboxylic acids resulting from the addition of alkaline metal compounds.[30] This was supported by the increase in CO_2 content in the gas phase. The reduction in aldehydes and ketones may be a consequence of the additives promoting decarboxylation or decarbonylation reactions.[31] The alkaline solution weakens the connection between lignin and the remaining hemicellulose, which contributes to a decrease in the relative concentration of ketones and ethers.[32] Furthermore, the reaction between alkaline compounds and acids or amines can also lead to a reduction in their respective concentrations.

Gas component analysis

Fig. 4 illustrates the compositional analysis of pyrolysis gas from the fast pyrolysis of WS. The syngas comprised CO_2 (32.6%), CO (31.7%), CH_4 (14.1%), H_2 (2.5%), and small hydrocarbons (C_2H_4, C_2H_6, and C_3H_8, labeled as "others"). The addition of alkali metal compounds to WS increased CO_2 and H_2 content. H_2 content in WS, WS–LC, WS–SC, WS–PC, and WS–PH were 2.5%, 3.45%, 4.83%, 12.75%, and 25.05%, respectively. CO and CH_4 content showed minimal change, with a slight increase in light hydrocarbons. The elevated CO_2 content may be attributed to the cleavage and rearrangement of the carboxyl and carbonyl groups;[33,34] this could also be due to the interaction of salts with steam (eqn (9)). The water–gas shift reaction can also contribute to the CO conversion to CO_2 (eqn (10)). Despite carbonate decomposition generating CO_2, it might not apply here, given that carbonate decomposition temperatures typically exceed 700 °C.[35,36] The increase in H_2 content can be attributed to two main factors. The first is the result of the dehydrogenation, condensation, and aromatization of organic matter and the cyclization of hydrocarbon compounds. These reactions lead to the generation of H_2 during pyrolysis. Secondly, alkali metal ions can react with the carboxyl (–COOH) or hydroxyl (–OH) groups in the volatile fraction, promoting the release of H_2 (eqn (11) and (12)).[34,37] Increased H_2 content is beneficial for the efficient and environmentally friendly utilization of pyrolysis gases. CO primarily originates from the cracking of ketones, ethers, and oxygen-containing heterocycles, while CH_4 and light hydrocarbons result mainly from the cleavage of methyl, methylene, and methoxy groups.[33,38]

$$M_2CO_3 + H_2O \rightarrow 2MOH + CO_2 \quad (9)$$

$$CO + H_2O \rightarrow CO_2 + H_2 \quad (10)$$

$$M + –COOH \rightarrow –COOH + H^+ \quad (11)$$

$$M^+ + –OH \rightarrow –OM + H^+ \quad (12)$$

where *M* is a metal ion.

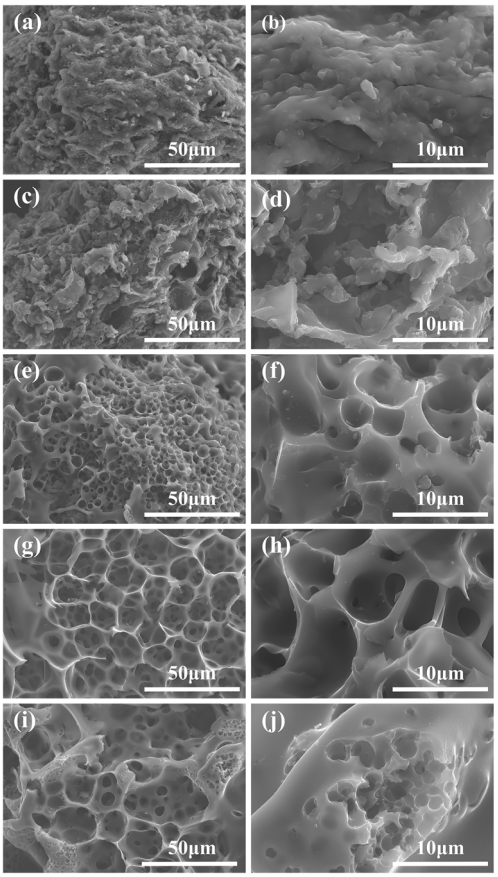

Fig. 5 SEM images of (a and b) WSC; (c and d) WSC–LC; (e and f) WSC–SC; (g and h) WSC–PC and (i and j) WSC–PH.

SEM analysis

Fig. 5 shows SEM images of carbon obtained from WS after pyrolysis and carbonization, with and without additives. The surface of WSC appeared rough, lacking distinct pore structures. WSC–LC exhibited a rougher surface with few pores, whereas WSC–SC had numerous non-interconnected pores. Furthermore, WSC–PC displayed relatively regular pore structures with clear interconnectivity. The addition of carbonates induced a more porous structure on the surface of the carbon material. The activation effect of carbonates is primarily achieved through three aspects. First, the obtained material undergoes etching, leading to the formation of the corresponding pore structures. For example, the reaction between carbonates (PC) and carbon (C) (eqn (13) and (14)) contributes to this process. As the oxidative nature of alkali metal ions increases, their reactivity with C also increases. The order of the metal oxidative nature, from highest to lowest, was $K^+ > Na^+ > Li^+$. Consequently, the abundance sequence of pore structures was PC > SC > LC. Second, the produced CO or CO_2 escapes along with the gases generated during the carbonization of the WS, further creating internal pores. Third, during acid washing with HCl solution and subsequent rinsing with distilled water, the removal of metallic solid substances that act as hard templates may aid in the formation of interconnected porous structures.[39] WSC–PH also featured a porous structure, and its pore-formation mechanism was similar to that of the previously mentioned carbonate (K_2CO_3). During the reaction, KOH is converted into K_2CO_3, K_2O, and CO (eqn (13)–(15)). Furthermore, at approximately 700 °C, the produced K atoms move within the carbon microcrystals, facilitating the activation and pore formation process.[40]

$$K_2CO_3 + C \rightarrow K_2O + 2CO \quad (13)$$

$$K_2O + C \rightarrow K + CO \quad (14)$$

$$6KOH + 2C \rightarrow 2K + 3H_2 + 2K_2CO_3 \quad (15)$$

BET analysis

The N_2 adsorption–desorption isotherms of the obtained carbon materials are shown in Fig. 6a. All isotherms exhibited Type I behavior, indicating that they were predominantly composed of microporous materials. At low relative pressures (P/P_0 < 0.1), the N_2 adsorption capacity of carbon sharply increased, confirming abundant micropores in WSC, WSC–LC, WSC–SC, WSC–PC, and WSC–PH.[41] Notably, WSC–PC and WSC–PH exhibited significantly higher quantities of micropores than WSC. The pore-size distribution analysis in Fig. 6b further supports these findings, revealing the majority of pore sizes below 1 nm, with a significant portion in the ultramicropore range (approximately 0.5 nm).[19,42] When the relative pressure approaches 0.1, the adsorption isotherms plateau. With increasing relative pressure, the adsorption volume gradually

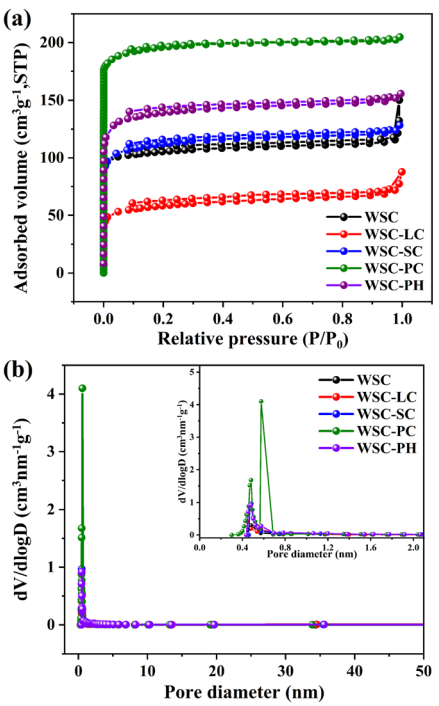

Fig. 6 (a) N_2 adsorption–desorption isotherms and (b) pore size distributions of WSC and WSC–X (X = LC, SC, PC and PH).

Table 2 Structural parameters of WSC, WSC–X (X = LC, SC, PC and PH)

Samples	S_{BET} (m^2 g^{-1})	V_{total} (cm^3 g^{-1})	V_{micro} (cm^3 g^{-1})	V_{micro}/V_{total} (%)	D (nm)
WSC	322.6	0.22	0.16	73	2.69
WSC–LC	182.5	0.12	0.09	75	2.64
WSC–SC	347.9	0.2	0.17	85	2.27
WSC–PC	598.6	0.32	0.3	94	2.11
WSC–PH	427.0	0.24	0.22	92	2.24

increases at a slower rate and displays hysteresis loops in the range of 0.1 to 0.9, indicating larger micropores and some mesoporous structures in the carbon materials.[43] As P/P_0 approaches 1.0, a small tail appears at the end of the adsorption isotherm, indicating the presence of macropores in the carbon material.[44]

Table 2 lists the pore structure parameters of the carbon materials. The specific surface area and total pore volume of WSC–PC were significantly higher than those of the other samples, reaching 598.6 m^2 g^{-1} and 0.32 cm^3 g^{-1}, respectively. Micropore proportions for WSC, WSC–LC, WSC–SC, WSC–PC, and WSC–PH were 73%, 75%, 85%, 94%, and 92%, respectively. These abundant micropores offer numerous ion adsorption sites, significantly enhancing material-specific capacitance. The formation of micropores is attributed to the etching effect of the activating agent on the carbon framework and the reaction between C and CO_2.[45] Compared to WSC, WSC–PC and WSC–PH exhibited increased specific surface area, total pore volume, and micropore volume, along with reduced average pore size, indicating that PC and PH induce the formation of microporous structures in the WSC carbonization process.[46]

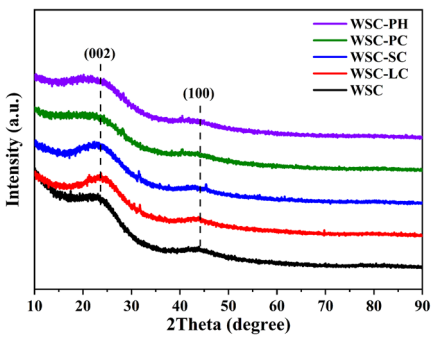

Fig. 7 XRD plots of WSC and WSC–X (X = LC, SC, PC and PH).

Table 3 Crystallite parameters from analysis of XRD for WSC, WSC–LC, WSC–SC, WSC–PC, WSC–PH

Samples	d_{002} (Å)	L_c (Å)	L_a (Å)
WSC	3.82	15.35	33.14
WSC–LC	3.76	12.78	40.63
WSC–SC	3.81	11.54	47.64
WSC–PC	3.99	10.32	46.69
WSC–PH	3.98	10.43	44.78

XRD and Raman analyses

The structural properties of carbon materials were characterized using X-ray diffraction spectroscopy, as shown in Fig. 7. All the samples exhibited two distinct diffraction peaks at approximately 23° and 43°. The diffraction peaks exhibited low heights and broad widths, indicating small grain size, low crystallinity, and an amorphous carbon structure.[47] In order to further reveal the differences in disorder and crystallinity between the materials, the layer spacing, and average grain size were calculated by Bragg's formula and Scherrer's formula. Table 3 summarizes the crystal parameters of the XRD analyses of the materials, from which it can be seen that the layer spacing of all materials (d_{002}) is larger than that of graphite (3.34 Å), indicating that the materials have a typical disordered structure.[48] In addition, the crystal size of the carbon material changed in some directions after the additives were added during the pyrolysis process, which can be seen from the decrease and increase of L_c and L_a, respectively.

To further investigate the structural characteristics of carbon materials, Raman spectroscopy was performed on the samples (Fig. 8), All samples exhibited two characteristic peaks associated with carbon materials. The D-band, located at approximately 1330 cm^{-1}, was primarily attributed to structural defects, whereas the G-band, located at approximately 1580 cm^{-1}, was mainly attributed to sp^2 hybridized carbon in the graphite framework of the biochar.[49] The I_D/I_G ratio, representing the intensity ratio of the D-band to the G-band, is commonly employed to evaluate the extent of defects and graphitization in graphitic carbon materials. A higher I_D/I_G ratio indicates a greater number of defects and a lower level of graphitization.[50] In the current investigation, the calculated I_D/I_G values for WSC, WSC–LC, WSC–SC, WSC–PC, and WSC–PH

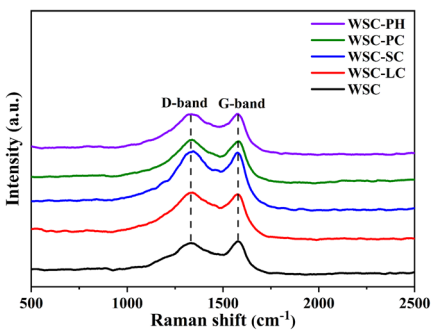

Fig. 8 Raman plots of WSC and WSC–X (X = LC, SC, PC and PH).

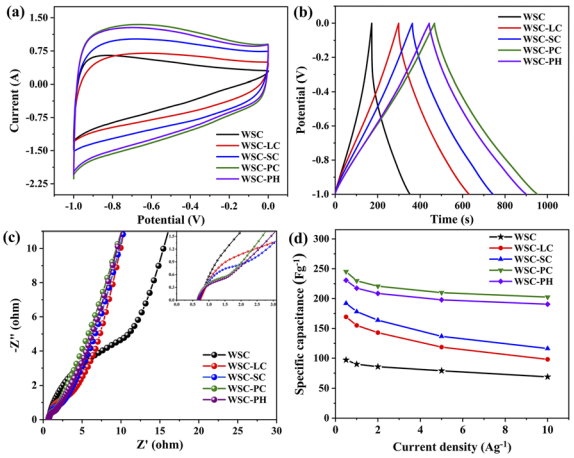

Fig. 9 (a) CV curves (5 mV s^{-1}), (b) GCD curves (0.5 A g^{-1}), (c) Nyquist plots and (d) specific capacitance at different current densities for WSC and WSC–X (X = LC, SC, PC and PH).

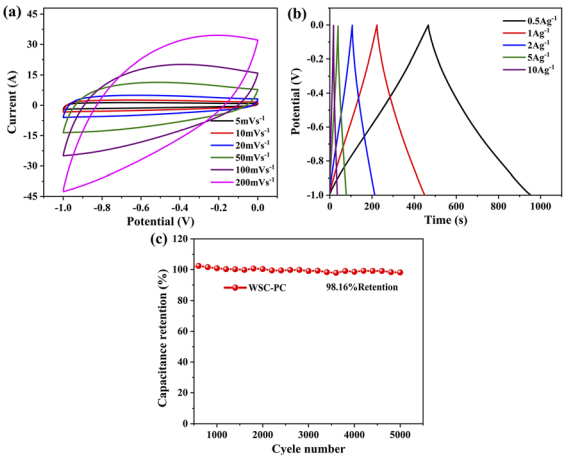

Fig. 10 Electrochemical performance of WSC–PC (a) CV curves at different scan rates from 5 to 200 mV s^{-1}; (b) GCD curves at current densities from 0.5 to 10 A g^{-1}; (c) cycling performance at 2 A g^{-1}.

were 0.98, 1.02, 1.03, 1.04, and 1.00, respectively. Therefore, WSC–PC exhibited the highest level of defect structure, consistent with the result of the N_2 adsorption–desorption isotherm test, which showed that WSC–PC has the largest specific surface area.

Electrochemical property analysis

To further investigate the influence of additives on the electrochemical performance of WSC, CV tests were conducted on the resulting carbon materials, as shown in Fig. 9a. The CV curves of WSC–LC, WSC–SC, WSC–PC, and WSC–PH exhibited rectangular shapes with larger integrated areas than those of WSC, indicating excellent double-layer capacitance. Constant-current charge–discharge curves exhibited no significant internal resistance drop for WSC–LC, WSC–SC, WSC–PC, and WSC–PH compared to WSC, showcasing good reversibility and double-layer capacitance when used as electrode materials (Fig. 9b). Calculatins from GCD discharge curves at a current density of 0.5 A g^{-1} yielded specific capacitances for WSC, WSC–LC, WSC–SC, WSC–PC, and WSC–PH, determined as 97.08, 169.32, 192.07, 245.18, and 230.72 F g^{-1}, respectively. Notably, WSC–PC exhibited the highest specific capacitance among the samples tested. Table 4 compares the previously reported commercial carbon with the carbon materials obtained in this paper, and the results show that the carbon prepared in this paper has excellent electrochemical properties.

Fig. 9c displays the Nyquist plots of WSC and WSC–X, displaying semicircles at high frequencies (negligible) and straight lines at low frequencies. In the high-frequency region, equivalent series resistances for WSC, WSC–LC, WSC–SC, WSC–PC, and WSC–PH were 0.72, 0.73, 0.70, 0.65, and 0.66 Ω, respectively. Therefore, WSC–PC displayed the lowest equivalent series resistance among the samples, with its electrode material exhibiting the smallest semicircular arc, indicative of the lowest charge transfer resistance (R_{ct}) and a fast interfacial charge transfer rate.

As shown in Fig. 9d, with increasing current density, the specific capacitance of all samples decreased due to insufficient time for the electrolyte ions to diffuse fully into material pores at higher current densities, resulting in less charge accumulation and a decrease in the specific capacitance. Notably, WSC–PC and WSC–PH exhibited a smaller decrease in specific capacitance with increasing current density. At a current density of 10 A g^{-1}, their specific capacitance remained at 83% of the initial capacitance at 0.5 A g^{-1}, indicating excellent rate performance.

Table 4 Comparison of electrochemical properties of reported commercial carbons and the carbons obtained in this paper

Materials	C_m (F g^{-1})	Measure condition	Electrolyte	Ref.
Carbon N0	93	5 mV s^{-1}	6 M KOH	51
YP-50F	122	0.1 A g^{-1}	6 M KOH	52
AC-C-1	164.49	5 mV s^{-1}	6 M KOH	53
AC	118	1 mV s^{-1}	1 M EMIM BF4/PC	54
AC	117	1 A g^{-1}	3 M KOH	55
CPC	100	0.625 A g^{-1}	6 M KOH	56
WSC–LC	169.32	0.5 A g^{-1}	6 M KOH	This work
WSC–SC	192.07	0.5 A g^{-1}	6 M KOH	This work
WSC–PC	245.18	0.5 A g^{-1}	6 M KOH	This work
WSC–PH	230.72	0.5 A g^{-1}	6 M KOH	This work

Owing to the outstanding performance of the WSC–PC in various aspects, an in-depth electrochemical performance test was conducted, Fig. 10a demonstrates that as the scan rate increased, the CV curve of WSC–PC gradually deviated from a rectangular shape, attributed to the difficulty of electrolyte ions reaching the electrode interface to form a double layer at high scan rates. Fig. 10b demonstrates that even at a high current density of 10 A g^{-1}, the GCD curve of WSC–PC maintained a symmetrical triangular shape, indicating a fast electrochemical response and excellent electrochemical reversibility.[50] The cyclic performance of WSC–PC at a current density of 2 A g^{-1} is shown in Fig. 10c, After 5000 cycles, the capacitance retention of WSC–PC remained at 98.16%, indicating excellent electrochemical stability and high reversibility of the material during constant current charge–discharge processes.

Conclusions

In this study, a one-step process that combined catalytic biomass pyrolysis with carbon activation was proposed. Alkali metal carbonates (LC, SC and PC) and PH are mixed with WS in certain proportions to achieve simultaneous catalytic pyrolysis and carbonization activation in a one-step process. The results indicated that the addition of LC, SC, PC, and PH enhanced secondary tar cracking, increasing yields of solid and gaseous products while reducing liquid yield. The phenolic content of the bio-oil significantly increased, whereas the levels of ketones, acids, and amines decreased. Simultaneously, the H_2 content of the pyrolysis gas increased significantly. For example, with the addition of PC, the phenolic content of the bio-oil increased from 47.26% to 74.9%, whereas the levels of ketones, acids, and amines decreased from 20.27%, 2.44%, and 3.5% to 10.73%, 0.34%, and 1.43%, respectively. The H_2 content in the pyrolysis gas increased from 2.5% in the case of individual pyrolysis to 12.75%. Furthermore, LC, SC, PC, and PH led to an increase in the surface defect structures and the formation of numerous micropores on the carbon; this facilitated more active sites for electrochemical reactions, resulting in a significant improvement in the electrochemical performance of carbon. Notably, the addition of PC resulted in the most remarkable enhancement in the performance of the resulting char. The specific capacitance of WSC–PC was determined to be 245.18 F g^{-1} at a current density of 0.5 A g^{-1}. Even at the high current density of 10 A g^{-1}, the specific capacitance remained at 83% of its initial value at 0.5 A g^{-1}. After 5000 charge–discharge cycles at a current density of 2 A g^{-1}, WSC–PC demonstrated a capacity retention rate of 98.16%. These findings underscore the remarkably high specific capacitance, excellent rate performance, and exceptional cycling stability of WSC–PC. In summary, this study integrated biomass catalytic pyrolysis and biochar activation processes, resulting in an enhanced quality of bio-oil and gas and improved carbon performance. This approach holds promise for the efficient and clean utilization of biomass.

Author contributions

Wenjing He: conceptualization, writing – original draft, writing – review & editing, supervision, funding acquisition. Keling Liu: conceptualization, writing – original draft, investigation, data curation. Lanjun Zhang: supervision, funding acquisition. Muxin Liu: conceptualization, supervision, funding acquisition. Zhengjie Ni: investigation, data curation. Yueyang Li: investigation, data curation. Duoduo Xu: investigation, data curation. Minjie Cui: investigation. Yibo Zhao: conceptualization, writing – review & editing, supervision, funding acquisition.

Conflicts of interest

There are no conflicts to declare.

Acknowledgements

This work was supported by the National Natural Science Foundation of China [grant numbers 21978003, and 52004104], the Open-end Funds of the Jiangsu Key Laboratory of Function Control Technology for Advanced Materials, Jiangsu Ocean University [grant number jsklfctam202002], the Postgraduate Research & Practice Innovation Program of Jiangsu Ocean University [grant numbers KYCX2022-38 and KYCX2022-01], and the Qinglan Project of Jiangsu Province.

Notes and references

1 S. V. Vassilev, C. G. Vassileva and V. S. Vassilev, *Fuel*, 2015, **158**, 330–350.
2 Y. Chen, Y. Yang, X. Liu, X.-y. Shi, C.-l. Wang, H. Zhong and F.-m. Jin, *Mol. Catal.*, 2023, **545**, 113199.
3 S.-s. Long, Y.-c. Feng, B.-l. Chen, L.-h. Gan, X.-h. Zeng, M.-n. Long and J. Liu, *Mol. Catal.*, 2023, **541**, 113106.
4 C. Manochio, B. R. Andrade, R. P. Rodriguez and B. S. Moraes, *Renewable Sustainable Energy Rev.*, 2017, **80**, 743–755.
5 C. Dolle, N. Neha and C. Coutanceau, *Curr. Opin. Electrochem.*, 2022, **31**, 100841.
6 M. Hamza, M. Ayoub, R. B. Shamsuddin, A. Mukhtar, S. Saqib, I. Zahid, M. Ameen, S. Ullah, A. G. Al-Sehemi and M. Ibrahim, *Environ. Technol. Innovation*, 2021, **21**, 101200.
7 L. C. Maia, L. C. Soares and L. V. Alves Gurgel, *J. Environ. Manage.*, 2021, **288**, 112397.
8 J. Gopalan, A. Buthiyappan and A. A. Abdul Raman, *J. Ind. Eng. Chem.*, 2022, **113**, 72–95.
9 M. Shanmuga Priya, P. Divya and R. Rajalakshmi, *Sustainable Chem. Pharm.*, 2020, **16**, 100243.
10 T. V. Nguyen and L. R. Clausen, *Energy Convers. Manage.*, 2019, **184**, 539–558.
11 L.-q. Zhang, S.-s. Li, K. Li and X.-f. Zhu, *Energy Convers. Manage.*, 2018, **166**, 260–267.
12 Y. Chen, H. Yang, X. Wang, S. Zhang and H. Chen, *Bioresour. Technol.*, 2012, **107**, 411–418.
13 M. Wang, S.-l. Zhang and P.-g. Duan, *Energy Sources, Part A*, 2019, **45**, 2637–2650.
14 K. Cen, J. Zhang, Z. Ma, D. Chen, J. Zhou and H. Ma, *Bioresour. Technol.*, 2019, **278**, 26–33.
15 W.-h. Zhou, B. Bai, G.-y. Chen, L.-l. Ma and B.-b. Yan, *Int. J. Hydrogen Energy*, 2019, **44**, 15863–15870.

16 C. Tirapanampai, W. Phetwarotai and N. Phusunti, *J. Anal. Appl. Pyrolysis*, 2019, **142**, 104644.
17 Y.-f. Shen, N.-y. Zhang and S. Zhang, *Energy*, 2020, **190**, 116431.
18 B. Jia, Q.-h. Mian, D.-l. Wu and T. Wang, *Mater. Today Chem.*, 2022, **24**, 100828.
19 Z.-b. Fu, K. Sun, H.-l. Fan, C. Li, H. Liu, S. Zhang, K. Ding, G.-g. Gao and X. Hu, *J. Cleaner Prod.*, 2022, **357**, 131936.
20 X.-f. Zhu, M.-z. Sun, X.-z. Zhu, W.-w. Guo, Z.-j. Luo, W.-f. Cai and X.-f. Zhu, *Fuel*, 2023, **334**, 126565.
21 G. Lin, Q. Wang, X. Yang, Z. Cai, Y. Xiong and B. Huang, *RSC Adv.*, 2020, **10**, 17768–17776.
22 N. Zhang and Y. Shen, *Bioresour. Technol.*, 2019, **284**, 332532.
23 W.-j. He, G.-j. Yin, Y.-b. Zhao, L.-j. Zhang, S.-y. Xu, T.-t. Huang, L. Chang and H.-x. Lu, *Fuel*, 2021, **302**, 121098.
24 C. Nita, B. Zhang, J. Dentzer and C. Matei Ghimbeu, *J. Energy Chem.*, 2021, **58**, 207–218.
25 J. S. Malhotra, R. Valiollahi and H. Wiinikka, *J. Energy Storage*, 2023, **57**, 106179.
26 M. Hu, Z. Ye, Q. Zhang, Q. Xue, Z. Li, J. Wang and Z. Pan, *Energy*, 2022, **245**, 123286.
27 M.-q. Chen, X.-y. Qi, J. Wang, M.-g. Chen, F.-f. Min, S.-m. Liu and B. Jing, *J. Fuel Chem. Technol.*, 2011, **39**, 585–589.
28 D. Nowakowski, J. Jones, R. Brydson and A. Ross, *Fuel*, 2007, **86**, 2389–2402.
29 S.-s. Li, C. Wang, Z.-j. Luo and X.-f. Zhu, *Energy Fuels*, 2020, **34**, 12654–12664.
30 Y.-p. Xie, K. Zeng, G. Flamant, H.-p. Yang, N. Liu, X. He, X.-y. Yang, A. Nzihou and H.-p. Chen, *Energy*, 2019, **179**, 1124–1132.
31 C. Peng, G.-y. Zhang, J.-r. Yue and G.-w. Xu, *Fuel Process. Technol.*, 2014, **124**, 212–221.
32 N. A. A. Rahman, F. Cardenas-Lizana and A. Sanna, *Catalysts*, 2023, **13**, 1122.
33 S.-q. Fang, X.-r. Wang, P. Li, J. Bai, C. Chang, X.-h. Wang, J.-d. Song and S.-s. Pang, *Fuel*, 2023, **333**, 126216.
34 K. Zeng, X.-y. Yang, Y.-p. Xie, H.-p. Yang, J. Li, D. Zhong, H.-y. Zuo, A. Nzihou, Y.-J. Zhu and H.-p. Chen, *Fuel*, 2021, **302**, 121103.
35 S. Yoshida, J. Matsunami and Y. Hosokawa, *Energy Fuels*, 1999, **13**, 961–964.
36 L. Shi, T. Qu, D. Liu, Y. Deng, B. Yang and Y. Dai, in *Materials Processing Fundamentals 2020*, 2020, ch. 10, pp. 107–116, DOI: **10.1007/978-3-030-36556-1_10**.
37 L. Ding, Z.-j. Zhou, Q.-h. Guo, W. Huo and G.-s. Yu, *Fuel*, 2015, **142**, 134–144.
38 Z.-q. Ma, Q.-f. Sun, J.-w. Ye, Q.-f. Yao and C. Zhao, *J. Anal. Appl. Pyrolysis*, 2016, **117**, 116–124.
39 G.-g. Song, J. Yang, K.-x. Liu, Z. Qin and X.-c. Zheng, *Diamond Relat. Mater.*, 2021, **111**, 108162.
40 W. Chen, M. Gong, K.-x. Li, M.-w. Xia, Z.-q. Chen, H.-y. Xiao, Y. Fang, Y.-q. Chen, H.-p. Yang and H.-p. Chen, *Appl. Energy*, 2020, **278**, 115730.
41 G.-x. Han, J.-b. Jia, Q.-r. Liu, G.-x. Huang, B. Xing, C.-x. Zhang and Y.-j. Cao, *Carbon*, 2022, **186**, 380–390.
42 X. Liu, C. Ma, J. Li, B. Zielinska, R. J. Kalenczuk, X. Chen, P. K. Chu, T. Tang and E. Mijowska, *J. Power Sources*, 2019, **412**, 1–9.
43 F. Jiao, H.-y. Sang, P. Guo, P. Miao and X.-x. Wang, *Chem. Phys. Lett.*, 2022, **803**, 139831.
44 A. A. Mohammed, C. Chen and Z. Zhu, *J. Colloid Interface Sci.*, 2019, **538**, 308–319.
45 F.-q. Guo, X.-c. Jiang, X.-p. Jia, S. Liang, L. Qian and Z.-h. Rao, *J. Electroanal. Chem.*, 2019, **844**, 105–115.
46 W.-d. Lei, B.-k. Yang, Y.-j. Sun, L.-w. Xiao, D.-y. Tang, K. Chen, J. Sun, J. Ke and Y. Zhuang, *J. Power Sources*, 2021, **488**, 229455.
47 J.-r. Wang, F. Wan, Q.-f. Lü, F. Chen and Q.-l. Lin, *J. Mater. Sci. Technol.*, 2018, **34**, 1959–1968.
48 F.-x. Wang, S.-y. Xiao, Y.-y. Hou, C.-l. Hu, L.-l. Liu and Y.-p. Wu, *RSC Adv.*, 2013, **3**, 13059.
49 S. Rawat, T. Boobalan, M. Sathish, S. Hotha and B. Thallada, *Biomass Bioenergy*, 2023, **171**, 106747.
50 S.-j. Zhang, X.-x. Ma, Y.-l. Du, Y.-t. Li, J. Lin and S.-l. Chen, *Adv. Powder Technol.*, 2023, **34**, 104221.
51 G. Lota, T. A. Centeno, E. Frackowiak and F. Stoeckli, *Electrochim. Acta*, 2008, **53**, 2210–2216.
52 Y.-h. Liu, X.-x. Qu, G.-x. Huang, B.-l. Xing, Y.-f. Fan, C.-x. Zhang and Y.-j. Cao, *J. Energy Storage*, 2021, **43**, 103200.
53 K. Zhang, J.-m. Sun, L. E, C.-h. Ma, S. Luo, Z.-w. Wu, W. Li and S.-x. Liu, *J. Energy Storage*, 2022, **45**, 103457.
54 S. Zhang, X.-z. Shi, R. Wróbel, X.-c. Chen and E. Mijowska, *Electrochim. Acta*, 2019, **294**, 183–191.
55 D. Wang, Z.-y. Fu, Y.-b. Xu, X.-l. Guo, F. Wang, W.-j. Sun, P. Yin, Z.-l. Yang and L.-x. Yang, *Mater. Lett.*, 2020, **281**, 128610.
56 L.-y. Pang, B. Zou, Y.-c. Zou, X. Han, L.-y. Cao, W. Wang and Y.-p. Guo, *Colloids Surf., A*, 2016, **504**, 26–33.